

# Spectrally balanced detection for optical frequency domain imaging

Yueli Chen, Daniel M. de Bruin, Charles Kerbage, and Johannes F. de Boer

Harvard Medical School and Wellman Center for Photomedicine, Massachusetts General Hospital  
50 Blossom Street, Boston, Massachusetts 02114

[ychen25@partners.org](mailto:ychen25@partners.org), [deboer@helix.mgh.harvard.edu](mailto:deboer@helix.mgh.harvard.edu)

**Abstract:** In optical frequency domain imaging (OFDI) or swept-source optical coherence tomography, balanced detection is required to suppress relative intensity noise (RIN). A regular implementation of balanced detection by combining reference and sample arm signal in a 50/50 coupler and detecting the differential output with a balanced receiver is however, not perfect. Since the splitting ratio of the 50/50 coupler is wavelength dependent, RIN is not optimally canceled at the edges of the wavelength sweep. The splitting ratio has a nearly linear shift of 0.4% per nanometer. This brings as much as  $\pm 12\%$  deviation at the margins of wavelength-swept range centered at 1060nm. We demonstrate a RIN suppression of 33dB by spectrally corrected balanced detection, 11dB more than regular balanced detection.

©2007 Optical Society of America

**OCIS codes:** (110.4500) Optical coherence tomography; (120.3180) Interferometry; (140.3600) Lasers, tunable; (170.3880) Medical and biological imaging;

---

## References and links

1. D. Huang, E. A. Swanson, C. P. Lin, J. S. Schuman, W. G. Stinson, W. Chang, M. R. Hee, T. Flotte, K. Gregory, C. A. Puliafito, and J. G. Fujimoto, "Optical Coherence Tomography," *Science* **254**, 1178-1181 (1991).
2. A. F. Fercher, C. K. Hitzenberger, G. Kamp, and S. Y. El-Zaiat, "Measurement of intraocular distances by backscattering spectral interferometry," *Opt. Commun.* **117**, 43-48 (1995).
3. S. R. Chinn, E. A. Swanson, and J. G. Fujimoto, "Optical coherence tomography using a frequency-tunable optical source," *Opt. Lett.* **22** (1997).
4. T. Mitsui, "Dynamic range of optical reflectometry with spectral interferometry," *Japanese Journal of Applied Physics Part 1-Regular Papers Short Notes & Review Papers* **38**, 6133-6137 (1999).
5. R. Leitgeb, C. K. Hitzenberger, and A. F. Fercher, "Performance of fourier domain vs. time domain optical coherence tomography," *Opt. Express* **11**, 889-894 (2003).
6. J. F. de Boer, B. Cense, B. H. Park, M. C. Pierce, G. J. Tearney, and B. E. Bouma, "Improved signal-to-noise ratio in spectral-domain compared with time-domain optical coherence tomography," *Opt. Lett.* **28**, 2067-2069 (2003).
7. M. A. Choma, M. V. Sarunic, C. H. Yang, and J. A. Izatt, "Sensitivity advantage of swept source and Fourier domain optical coherence tomography," *Opt. Express* **11**, 2183-2189 (2003).
8. M. Wojtkowski, R. Leitgeb, A. Kowalczyk, T. Bajraszewski, and A. F. Fercher, "In vivo human retinal imaging by Fourier domain optical coherence tomography," *J. Biomed. Opt.* **7**, 457-463 (2002).
9. N. A. Nassif, B. Cense, B. H. Park, M. C. Pierce, S. H. Yun, B. E. Bouma, G. J. Tearney, T. C. Chen, and J. F. de Boer, "In vivo high-resolution video-rate spectral-domain optical coherence tomography of the human retina and optic nerve," in *Opt. Express* (2004), pp. 367-376.
10. S. H. Yun, G. J. Tearney, J. F. de Boer, N. Itimbia, and B. E. Bouma, "High-speed optical frequency-domain imaging," *Opt. Express* **11**, 2953-2963 (2003).
11. B. Cense, N. Nassif, T. C. Chen, M. C. Pierce, S. H. Yun, B. H. Park, B. E. Bouma, G. J. Tearney, and J. F. de Boer, "Ultra-high-Resolution High-Speed Retinal Imaging Using Spectral-Domain Optical Coherence Tomography," *Opt. Express* **12**, 2435-2447 (2004).
12. M. A. Choma, K. Hsu, and J. A. Izatt, "Swept source optical coherence tomography using an all-fiber 1300-nm ring laser source," *J. Biomed. Opt.* **10** (2005).
13. B. Grajciar, M. Pircher, A. F. Fercher, and R. A. Leitgeb, "Parallel Fourier domain optical coherence tomography for in vivo measurement of the human eye," *Opt. Express* **13**, 1131-1137 (2005).

14. B. H. Park, M. C. Pierce, B. Cense, S. H. Yun, M. Mujat, G. J. Tearney, B. E. Bouma, and J. F. de Boer, "Real-time fiber-based multi-functional spectral-domain optical coherence tomography at 1.3  $\mu\text{m}$ ," *Opt. Express* **13**, 3931-3944 (2005).
15. W. Y. Oh, S. H. Yun, B. J. Vakoc, G. J. Tearney, and B. E. Bouma, "Ultrahigh-speed optical frequency domain imaging and application to laser ablation monitoring," *Appl. Phys. Lett.* **88** (2006).
16. B. R. White, M. C. Pierce, N. Nassif, B. Cense, B. H. Park, G. J. Tearney, B. E. Bouma, T. C. Chen, and J. F. de Boer, "*In vivo* dynamic human retinal blood flow imaging using ultra-high-speed spectral domain optical Doppler tomography," *Opt. Express* **11**, 3490-3497 (2003).
17. S. Yan, D. Piao, Y. Chen, and Q. Zhu, "Digital signal processor-based real-time optical Doppler tomography system," *Journal of biomedical optics* **9**, 454-463 (2004).
18. J. Zhang, and Z. P. Chen, "In vivo blood flow imaging by a swept laser source based Fourier domain optical Doppler tomography," *Opt. Express* **13**, 7449-7457 (2005).
19. W. Y. Oh, S. H. Yun, G. J. Tearney, and B. E. Bouma, "115 kHz tuning repetition rate ultrahigh-speed wavelength-swept semiconductor laser," *Opt. Lett.* **30**, 3159-3161 (2005).
20. R. Huber, M. Wojtkowski, and J. G. Fujimoto, "Fourier Domain Mode Locking (FDML): A new laser operating regime and applications for optical coherence tomography," *Opt. Express* **14**, 3225-3237 (2006).
21. R. Huber, D. C. Adler, and J. G. Fujimoto, "Buffered Fourier domain mode locking: unidirectional swept laser sources for optical coherence tomography imaging at 370,000 lines/s," *Opt. Lett.* **31**, 2975-2977 (2006).
22. S. H. Yun, G. J. Tearney, B. J. Vakoc, M. Shishkov, W. Y. Oh, A. E. Desjardins, M. J. Suter, R. C. Chan, J. A. Evans, I. K. Jang, N. S. Nishioka, J. F. de Boer, and B. E. Bouma, "Comprehensive volumetric optical microscopy in vivo," *Nature Medicine* **12**, 1429-1433 (2006).
23. T. C. Chen, B. Cense, M. C. Pierce, N. Nassif, B. H. Park, S. H. Yun, B. R. White, B. E. Bouma, G. J. Tearney, and J. F. de Boer, "Spectral domain optical coherence tomography: ultra-high speed, ultra-high resolution ophthalmic imaging," *Arch Ophthalmol* **123**, 1715-1720 (2005).
24. Y. Yasuno, V. D. Madjarova, S. Makita, M. Akiba, A. Morosawa, C. Chong, T. Sakai, K. P. Chan, M. Itoh, and T. Yatagai, "Three-dimensional and high-speed swept-source optical coherence tomography for in vivo investigation of human anterior eye segments," *Opt. Express* **13**, 10652-10664 (2005).
25. Y. Zhang, B. Cense, J. Rha, R. S. Jonnal, W. Gao, R. J. Zawadzki, J. S. Werner, S. Jones, S. Olivier, and D. T. Miller, "High-speed volumetric imaging of cone photoreceptors with adaptive optics spectral-domain optical coherence tomography," *Opt. Express* **14**, 4380-4394 (2006).
26. Y. Yasuno, Y. Hong, S. Makita, M. Yamanari, M. Akiba, M. Miura, and T. Yatagai, "In vivo high-contrast imaging of deep posterior eye by 1- $\mu\text{m}$  swept source optical coherence tomography and scattering optical coherence angiography," *Opt. Express* **15**, 6121-6139 (2007).
27. C. Kerbage, H. Lim, W. Sun, M. Mujat, and J. F. de Boer, "Large depth-high resolution full 3D imaging of the anterior segments of the eye using high speed optical frequency domain imaging," *Opt. Express* **15**, 7117-7125 (2007).
28. G. Hausler, and M. W. Lindner, "Coherence Radar and Spectral Radar - new tools for dermatological diagnosis," *J. Biomed. Opt.* **3**, 21-31 (1998).
29. R. Huber, M. Wojtkowski, J. G. Fujimoto, J. Y. Jiang, and A. E. Cable, "Three-dimensional and C-mode OCT imaging with a compact, frequency swept laser source at 1300 nm," *Opt. Express* **13**, 10523-10538 (2005).
30. H. Lim, M. Mujat, C. Kerbage, E. C. Lee, Y. Chen, T. C. Chen, and J. F. de Boer, "High-speed imaging of human retina in vivo with swept-source optical coherence tomography," *Opt. Express* **14**, 12902-12908 (2006).
31. N. Nassif, B. Cense, B. H. Park, S. H. Yun, T. C. Chen, B. E. Bouma, G. J. Tearney, and J. F. de Boer, "In vivo human retinal imaging by ultrahigh-speed spectral domain optical coherence tomography," *Opt. Lett.* **29**, 480-482 (2004).
32. W. V. Sorin, and D. M. Baney, "A Simple Intensity Noise-Reduction Technique for Optical Low-Coherence Reflectometry," *IEEE Photonics Technology Letters* **4**, 1404-1406 (1992).
33. B. M. Hoeling, A. D. Fernandez, R. C. Haskell, E. Huang, W. R. Myers, D. C. Petersen, S. E. Ungersma, R. Y. Wang, M. E. Williams, and S. E. Fraser, "An optical coherence microscope for 3-dimensional imaging in developmental biology," *Opt. Express* **6**, 136-146 (2000).
34. L. Mandel, and E. Wolf, "Measures of Bandwidth and Coherence Time in Optics," *Proceedings of the Physical Society of London* **80**, 894-897 (1962).
35. B. E. A. Saleh, and M. C. Teich, *Fundamentals of Photonics*, J. W. Goodman, ed. (John Wiley & Sons, Inc., New York, 1991), pp. 403-406.
36. E. C. W. Lee, J. F. de Boer, M. Mujat, H. Lim, and S. H. Yun, "In vivo optical frequency domain imaging of human retina and choroid," *Opt. Express* **14**, 4403-4411 (2006).
37. S. H. Yun, C. Boudoux, G. J. Tearney, and B. E. Bouma, "High-speed wavelength-swept semiconductor laser with a polygon-scanner-based wavelength filter," *Opt. Lett.* **28**, 1981-1983 (2003).

---

## 1. Introduction

Optical coherence tomography (OCT) is mostly used for biomedical subsurface imaging. It can be implemented by either time-domain or Fourier-domain architectures [1-3]. The latter has become more prevalent recently due to its extraordinary sensitivity advantage [4-7], which

can be readily transformed to higher acquisition speed. Fast frame rate is particularly valuable for biomedical imaging *in vivo* [8-22]. For example, in retina imaging, eye motion can be significantly reduced by faster acquisition, making *en face* imaging of vasculature and 3-D volumetric rendering feasible [23-27].

Fourier-domain OCT can be realized in two distinct implementations. In a spectral-domain design (SD-OCT), a spectrometer in the detection arm measures the spectrally resolved interference.[2, 28]. A Fourier transform of the spectrum generates a depth profile (A-line). Optical frequency domain imaging (OFDI) measures the spectrally resolved interference by rapidly tuning the source wavelength before it enters the interferometer such that the temporally encoded wavelength resolved signal can be detected with one single detector [10, 12, 15, 29, 30]. Recently, ultrahigh speed wavelength tuning techniques have been successfully implemented, resulting in A-line rates exceeding 100kHz using a polygon based tunable filter and 300kHz using a resonant fiber Fabry-Perot filter in a Fourier-domain mode locked laser [19-21].

In OFDI the use of laser source with a narrow instantaneous line width requires balanced detection to suppress relative intensity noise (RIN). However, the RIN suppression is found to be imperfect due to the spectrally dependent splitting ratio of 50/50 fiber coupler. Unlike SD-OCT[31], the theoretically predicted shot-noise-limited sensitivity is still not reached in OFDI. This can be attributed to a number of factors, such as incomplete RIN suppression and significant thermal noise (detector noise) for high bandwidth balanced detectors. We have observed consistently about 12dB difference between theoretical and experimentally measured sensitivity for a 1050 nm OFDI system.

In this paper, we have systematically analyzed and quantified the four major noise components, namely thermal, shot, RIN, and data acquisition noise in a 1050 nm OFDI system. It turned out that a shot-noise-limited window for the reference arm power does not exist with a regular balanced detection scheme. To improve the sensitivity, we implement a novel balanced detection technique. Instead of using the differential amplifier in the detector to balance the two output fiber leads, we digitize the two output channels separately and process the balanced detection in digital domain after correction of the spectrally dependent splitting ratio.

## 2. Principle

The detected signal current  $I_{det}(k)$  in our OFDI can be written as,

$$I_{det}(k) = I_{ref}(k) + I_s(k) + 2\sqrt{I_{ref}(k)I_s(k)} \cos(k \cdot z), \quad (1)$$

assuming a narrow instantaneous laser line width.  $I_{ref}$  and  $I_s$  are the detected reference and sample arm signal current.  $k$  is the wave vector and  $z$  is the depth with respect to the reference mirror. The third term in the right hand of Eq. 1 is the signal component pertaining to the depth information of the sample. The noise current however, is mainly coming from  $I_{ref}$  since  $I_{ref}$  is generally orders of magnitude larger than  $I_s$ . In OCT systems, there are three noise components (thermal, shot and RIN noise) that usually need to be properly addressed to optimize the system sensitivity [32, 33]. Thermal noise is related to the detector and is not a function of reference arm power. Shot noise arises from the discrete nature of the charge-carrying particles, the power of which is linearly proportional to the reference power. The shot noise power can be described as

$$\sigma_{shot}^2 = 2qI_{ref}, [A^2 / Hz] \quad (2)$$

where  $q$  is the electron charge. RIN is a property of the light source and is a common mode type of noise with the noise power proportional to the square of reference power. For black-body radiation, the RIN noise power is

$$\sigma_{RIN}^2 = 2\tau_{coh}I_{ref}^2, [A^2 / Hz] \quad (3)$$

where  $\tau_{coh}$  is the coherence time of the source. Assuming a Gaussian source with full width at half maximum line width of  $\Delta\lambda$ ,  $\tau_{coh} = \sqrt{2 \ln 2} / \pi \lambda_0^2 / (c \cdot \Delta\lambda)$  .[34] For a laser source with a certain line width, RIN noise can be much smaller than for black body radiation with a comparable bandwidth[35]. In our system, the data acquisition noise from the digitization board needs to be considered too. Finally, the over all system noise power is the summation of all noise sources

$$\sigma_{total}^2 = \sigma_{thermal}^2 + \sigma_{shot}^2 + \sigma_{RIN}^2 + \sigma_{daq}^2, [A^2 / Hz] \quad (4)$$

where the last term represents the noise of the data acquisition board. Short-noise-limited detection is the optimal situation where shot noise dominates over other noise sources. For a shot noise limited OFDI system, the best theoretical SNR is given by [5, 6, 10],

$$SNR = 10 \cdot \log\left(\frac{\eta P_s}{h\nu \cdot f_A}\right). \quad (5)$$

Here  $\eta$  and  $h\nu$  are the quantum efficiency coefficient and photon energy respectively and  $f_A$  is the A-line or wavelength tuning rate. The detected electrical signal current  $I_s$  is related to the sample arm optical power  $P_s$  by,

$$I_s = \frac{\eta q P_s}{h\nu}. \quad (6)$$

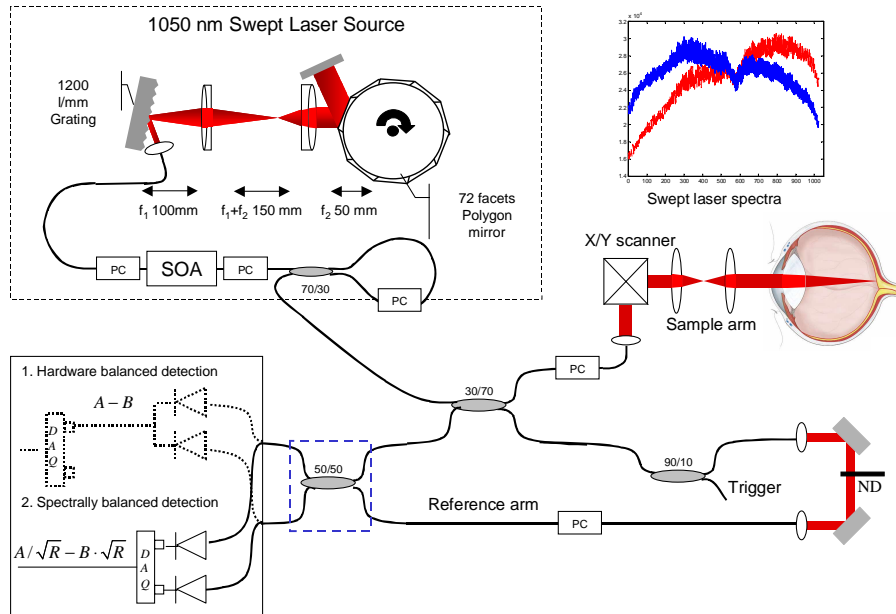


Fig. 1. Schematic of the 1050nm OFDI system. The wavelength-swept laser is on the top-left [36]. A mirror in the tunable mirror served as the end reflector that doubles the free spectral range[19]. The imaging interferometer uses a 30/70 fiber coupler to split sample and reference arm light. They recombined at a 50/50 coupler. The two balanced detection configurations are illustrated in the bottom-left corner. SOA: semiconductor optical amplifier, PC: Polarization controller. The inset (top-right) is the swept laser spectra from the two 50/50 coupler outputs where the 50/50 splitting ratio is only valid around the central wavelengths.

### 3. Experiments

#### 3.1 System configuration

The fiber-based 1050nm OFDI system was described previously [36]. The top left corner in Fig. 1 shows the schematic of the swept laser source. Light from a SOA is angularly dispersed by a diffraction grating. A two-lens telescope converges the light from the grating to the scanning polygon mirror. The polygon filter then selects a narrow pass band of light that is coupled back into the linear cavity to build the instantaneous laser output [37]. The 3dB bandwidth of the swept laser is 64nm with an output power of 6mW. The custom designed polygon has 72 facets and requires 2 input pulses per rotation. In the experiment, it is driven by a function generator at 820Hz, yielding an A-line rate about 30k. The interferometer configuration includes a 30/70 coupler. The sample arm is directed to a slit lamp with integrated XY scanner. The returned light recombines the reference arm light whose power is continuously adjustable by a neutral density filter. 10% of the reference arm light is coupled to a fiber grating which selects a fixed wavelength to synchronize the data acquisition.

At the detection port, a wideband 50/50 fiber coupler at 1050nm (AC Photonics) is selected for balanced detection. In a conventional balanced detection scheme, the two outputs from the 50/50 coupler are directed to a 2-channel balanced detector (New Focus 1817). The electrical signal is subsequently amplified with a build-in differential amplifier that produces a single-channel balanced output. Because of the spectrally dependent fiber splitting ratio (as seen from the output spectra on top-right of Fig. 1 and from Fig. 2), we implement another detection scheme where the two optical outputs are directed to two unbalanced detectors and digitized separately by a 2-channel, 100MHz data acquisition board with 14bit resolution (NI PCI-5122). The balanced detection is performed in the digital domain with an optimized balancing algorithm.

#### 3.2 Spectrally balanced detection

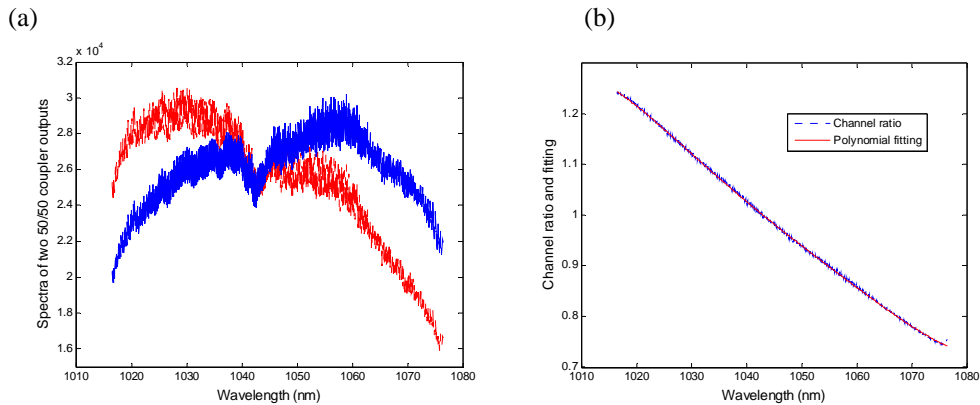


Fig. 2. (a) Digitized wavelength-sweep laser spectra from the two 50/50 coupler outputs. The 50/50 splitting ratio is exact only around central part of the spectra. (b) The spectrally dependent channel splitting ratio of the coupler (dotted blue) and the polynomial fitting (solid red). The fitting curve is used to compensate the spectral dependent splitting ratio and improve the effectiveness of balanced detection.

The detected optical signal from the two 50/50 coupler outputs for one wavelength sweep is shown in Fig. 2(a). Although a wideband coupler has been selected, the spectra in the two channels differ significantly. The 50/50 coupling only appears at the center of the spectrum with a maximum deviation over the wavelength sweep exceeding  $\pm 12\%$  (i.e. 44/56 instead of 50/50). Because the regular balanced detection uses a differential amplifier where the output is a direct subtraction of the two input signal, the common mode rejection ratio is critically

dependent on the identicalness of the two channels. The imperfect splitting ratio therefore impacts the balanced detection. To improve the RIN suppression the two channels were digitized separately. The ratio of the two channels is calculated and plotted in Fig. 2(b). The spectrally dependent splitting ratio is not dependent on other factors such as power level or spectral variation but an intrinsic property of the fiber coupler. A 5th order polynomial fit of the channel ratio  $R(\lambda) = S_{ch1}/S_{ch2}$  is used as a compensation function. The spectrally balanced detection is then performed in digital domain where  $R(\lambda)$  is used to scale the two channel signals over the full spectral range to the same magnitude before subtraction,

$$S_{bal}(\lambda) = S_{ch1}(\lambda) / \sqrt{R(\lambda)} - S_{ch2}(\lambda) \cdot \sqrt{R(\lambda)}. \quad (7)$$

### 3.3 Noise analysis

With conventional hardware balanced detection, we have scanned a range of reference arm powers by a neutral density filter to find the optimal power level. The best measured sensitivity was 12dB above the theoretical shot noise limit. To assess the system sensitivity and optimize the performance, we performed systematic experiments to delineate and quantify different noise sources in the OFDI system. In this paper, we have calculated the absolute noise power of different noise components based on the digitized noise spectra. Because the measured absolute value of the noise power depends on the amplification in the transimpedance amplifier and the DAQ board, all noise powers are calculated as noise current at the PIN detectors before the transimpedance amplifier to provide a universal reference point. The theoretical shot noise calculation of Eq. 2 can be directly used for this reference point. The noise power is presented as  $10 \log (\text{pA}^2/\text{Hz})$ . We computed noise spectra via an average of 1024 discrete Fourier transform of A-lines each with 1024 data points at 33MHz sampling rate. The noise levels were determined at a carrier frequency of 2.5MHz.

First, the thermal or detector noise was determined by measuring the dark current output from the detector when there is no optical input. The thermal noise included all optical power independent noise components of the detection system including system filter response. The noise level increased slightly at high frequency (Fig. 3). The thermal noise was measured at different vertical ranges of the data acquisition board. Fig. 3 shows that the thermal noise (blue curve) is not a constant at 1V, 2V and 4V data acquisition vertical ranges, demonstrating that the DAQ noise contributes to the thermal noise. The DAQ noise (red dotted curves) was determined by terminating the input to the digitization board with a 50-ohm impedance. It increased by 6dB when the vertical range doubles (in agreement with the digitizer manual). The analytic relation between noise levels at different vertical range is given by  $N_{dB,b} = N_{dB,a} + 20 \log (V_b / V_a)$ , where  $N_{dB,a}$  and  $N_{dB,b}$  are the noise levels at digitizer vertical voltage ranges  $V_a$  and  $V_b$ , respectively. The actual thermal noise is independent of DAQ vertical range after subtracting the DAQ noise from the measured noise spectrum. The thermal noise was  $7.8 \text{ pA}^2/\text{Hz}$ , corresponding to a noise equivalent power (NEP) of the detector of  $3.7 \text{ pW}/\sqrt{\text{Hz}}$  for a detector responsivity of  $R=0.75 \text{ A/W}$ . Compared with the minimum NEP =  $2.5 \text{ pW}/\sqrt{\text{Hz}}$  at low frequency specified in the detector manual, the larger measured value is most likely due to aliasing of noise above the Nyquist frequency. The build-in low-pass anti-aliasing filter of the NI board with a cut-off frequency 20MHz did not provide enough attenuation at or above the Nyquist frequency (16.5 MHz). We can also see that the DAQ noise level at 4V vertical range is actually higher than the thermal noise floor. Therefore, within the limitation of the available hardware, we will have to consider carefully four independent noise components in order to fully assess the total noise power.

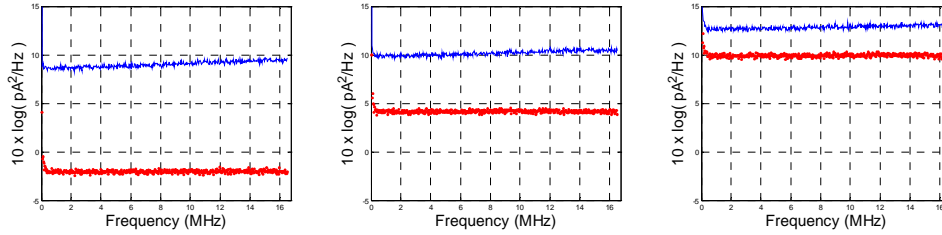


Fig. 3. The detection system noise consists of thermal and DAQ noise. Noise spectra were acquired in three data acquisition vertical ranges of 1, 2, and 4V peak-to-peak from left to right. Blue solid lines are the thermal plus DAQ noise measured when the optical input to the detector was blocked. Red dotted lines are DAQ noise when digitizer's analog input is terminated with 50 ohm. A discrete Fourier transform of 1024 data points is used to assess the noise floor. Y-axis is in absolute unit  $10\log(\text{pA}^2/\text{Hz})$  calculated at the PIN detector output.

Next the RIN noise level was determined. We measured the total noise in unbalanced, regular hardware balanced and spectrally balanced detection conditions for a range of reference arm power levels. The previously determined thermal and DAQ noise was subtracted from each measurement, which left only the contribution of shot and RIN noise. Since two detectors and digitization channels were used for the spectrally balanced scheme, two thermal and DAQ noise terms were subtracted. We then fit the remaining portion of the noise curve with  $N(I_{ref}) = 10 \cdot \log[ 2\eta q^2 P_{ref} / hv \cdot \gamma + P_{RIN} \cdot (\eta q P_{ref} / hv)^2 ]$  with  $P_{RIN}$  the only fit parameter. The quantum efficiency  $\eta$  calculated from the detector specification is 0.9. The first term in the logarithm bracket is shot noise (Eq. 2). A small adjustment factor  $\gamma$  is used to take into account the aliasing of noise above the Nyquist frequency. Our measured thermal noise power at 2.5MHz is 2.2 times larger than manufacture specification.  $(3.7 / 2.5 \text{ pW}/\sqrt{\text{Hz}})^2 = 2.2$ . The manufacturer specifications indicate that thermal noise at 100MHz (the maximum frequency estimated to contribute to the noise) is about 7 fold larger than the minimum value. Assuming a linear increment, the integrated thermal noise spectrum is about 4 times larger than an integrated white or shot noise spectrum. Therefore, the additional shot noise due to aliasing is estimated to be 30%, and  $\gamma$  equals 1.3. The second term is RIN, where  $P$  is the fitted RIN coefficient with unit second. The fitting results are shown in Fig. 4, where  $P_{RIN} = 7.488\text{e-}12$ ,  $4.69\text{e-}14$ , and  $3.53\text{e-}15$  respectively for unbalanced, hardware balanced, and spectrally balanced RIN. Note that the reference power level for single unbalanced detection is half that of the balanced schemes, where both channels are summed. By comparing  $10\log(P_{RIN})$ , the hardware balanced RIN level is about 22dB lower than unbalanced RIN. The spectral balancing scheme results in an additional 11 dB noise suppression from the hardware balanced RIN.

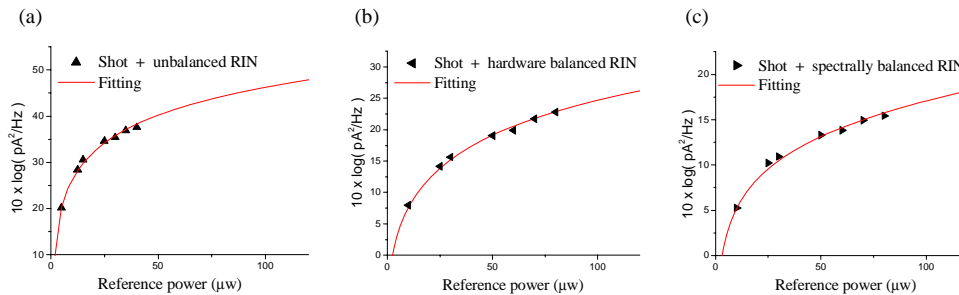


Fig. 4. Fitting of shot plus RIN noise in three detection conditions. (a) Unbalanced detection, (b) Regular hardware balanced detection, and (c) Spectrally balanced detection. The dotted plots are experimental noise measurement after removal of thermal and DAQ noise. The red solid lines are the nonlinear fit by Origin 6.

Figure 5 shows the contribution of each noise term. The DAQ noise appears as a step function corresponding to the different vertical range setting of 0.2, 0.4, 1, 2, 4, and 10V, respectively (from left to right). In the experiments, the smallest vertical range possible before saturation was always selected to minimize the effect of DAQ noise. Thermal noise was experimentally determined and is power independent. The shot noise curve is based on the theoretical prediction including the  $\gamma$  factor of 1.3. The RIN curves are based on the measured  $P_{RIN}$  values assuming a quadratic dependence on the reference arm power. The experimental results and fitting curves in Fig. 4 are also included in Fig. 5 for comparison. Dashed lines are the fitting curves and symbols are the measured shot plus RIN noise experimental data. The shot plus unbalanced RIN curve overlaps with the unbalanced RIN curve because unbalanced RIN dominates all other noise terms. The graph shows that for hardware balanced detection there is no shot noise limited window for the reference arm power where shot noise dominates all other noise terms. The noise analysis has revealed an 11 dB better RIN suppression of spectral balanced detection over hardware balanced detection. However, two separate unbalanced detectors are needed in the spectral balance scheme, adding one additional portion of thermal and DAQ noise. Nonetheless, as can be concluded from Fig. 5, a small window does appear where the shot noise is greater than the other noise contributions if spectral balanced detection could be implemented with a single detector.

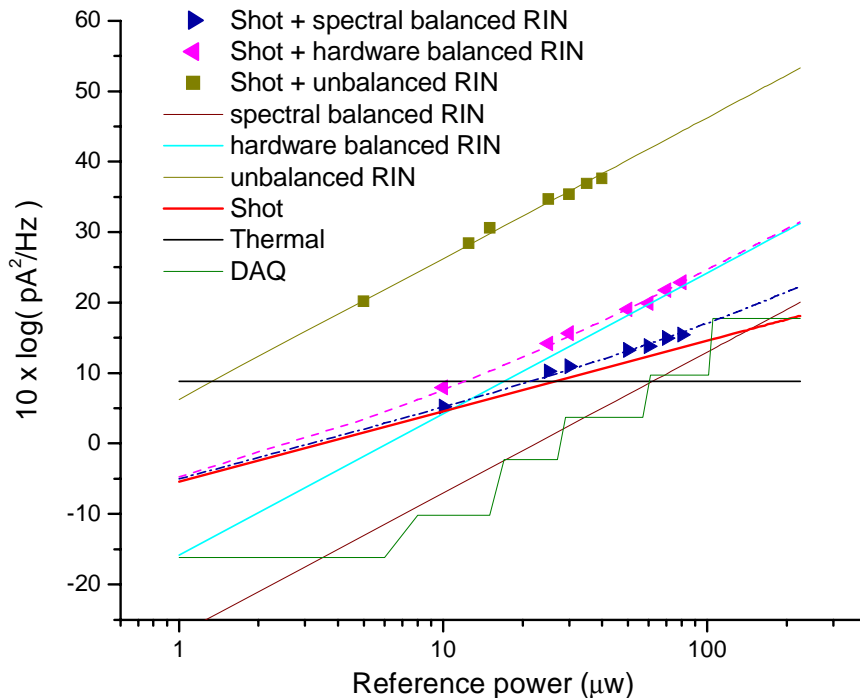


Fig. 5. The system noise characterization plotted as a function of the reference power for 1050nm OFDI after decomposition of four primary noise components: DAQ, thermal, shot, and RIN noise. The y-axis gives absolute noise power expressed as the noise current in decibel at the PIN detector. The symbols are experimental data, dashed lines are fits to the experimental data, and the solid lines are the decomposed four noise components. Hardware balanced detection suppressed about 22dB RIN. Spectral balance further suppressed 11dB. A reference power window where shot noise is larger than all other noise terms appears in spectral balanced detection. DAQ noise cannot be ignored especially at high digitizer vertical ranges (4V and 10V).

To demonstrate that spectral balanced detection can effectively suppress further the RIN noise in an OFDI system, a mirror was placed in the sample arm of the system, about 0.5mm away from the zero reference position. The optimal reference power, determined by the maximum power for which the digitizer did not saturate within the 2V vertical range, was  $50\mu\text{W}$ , about 4 times larger than the optimal power in the hardware balanced configuration. Figure 6(a) shows the depth profile for spectral balanced detection and Fig. 6(b) is processed by a direct subtraction of two DAQ channel data. The small peaks at high frequency are the fixed-pattern noise from the OFDI source and mixing terms with the mirror sample. The SNR benefit of spectral balanced detection can be seen in Fig. 6(c), which is the subtraction of the depth profile of Fig. 6(b) from 6(a). An overall 5-8 dB SNR improvement within the depth range of the system has been achieved, which is attributed to the 11 dB additional RIN suppression. The optimal reference power for hardware balanced detection with a *single* detector is  $15\mu\text{W}$ . In that case the system sensitivity is about 2 dB better than the sensitivity for a reference power of  $50\mu\text{W}$  with *two* detectors. Therefore the net sensitivity gain of spectral balancing with two detectors at  $50\mu\text{W}$  compared to hardware balancing with a single detector at  $15\mu\text{W}$  is about 3-6dB.

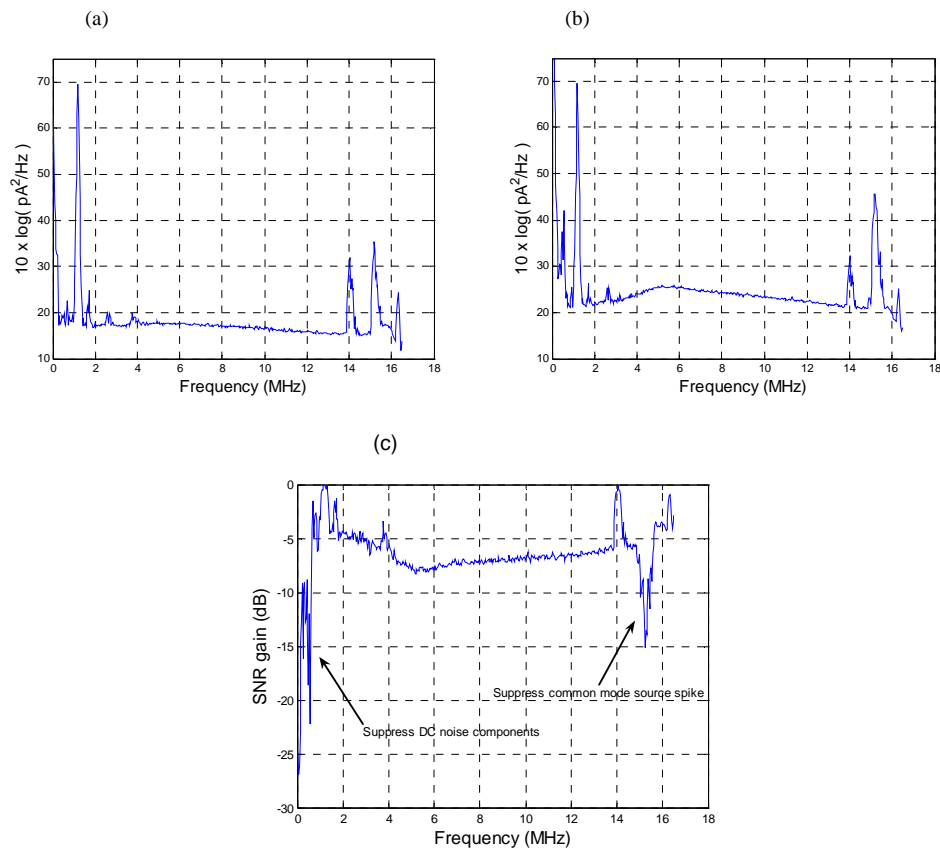


Fig. 6. (a) and (b) are the depth profiles of spectrally balanced and directly balanced detections schemes, respectively. The strong peak to the left is from a mirror sample about 0.5 mm away from the reference mirror. The peak to the right is from the laser source, and two sidelobes are the mixing terms of the mirror sample and the laser source peak. Fig 6 (c) shows the subtraction of the software balanced from the hardware balanced depth profile, demonstrating a 5-8 dB noise suppression. In addition, the DC and common mode source noise peak are also reduced. The two side peaks around the source peak are still at the same level because they arise from the mixing of sample mirror and laser source signal, which are not common mode signals.

Based on the detailed noise analysis, the noise levels can be calculated for the hardware balanced (HB) and Spectral balanced (SB) detection with 50 $\mu$ W reference arm power at a frequency of 2.5 MHz.

$$\sigma_{HB}^2 = 2 \times (\sigma_{Thermal}^2 + \sigma_{DAQ}^2) + \sigma_{shot}^2 + \sigma_{RIN,HB}^2 = 19.9 + 15.6 + 66.0 = 101.5 pA^2 / Hz \quad (8)$$

$$\sigma_{SB}^2 = 2 \times (\sigma_{Thermal}^2 + \sigma_{DAQ}^2) + \sigma_{shot}^2 + \sigma_{RIN,SB}^2 = 19.9 + 15.6 + 5.0 = 40.5 pA^2 / Hz$$

The measured noise reduction of ~5 dB at 2.5 MHz in Fig. 6(c) is slightly better than the predicted noise reduction  $10 \log(\sigma_{HB}^2 / \sigma_{SB}^2) = 4$  dB.

#### 4. Conclusion

We have systematically analyzed the thermal, DAQ, shot, and RIN noise of our 1050nm polygon filter based OFDI system. Based on the quantitative characterization of the four noise components, we demonstrate that spectrally balanced detection opens up a reference arm power window where shot noise is larger than other noise contributions. This is due to the 11dB better RIN suppression. The technique also more efficiently reduces the DC signal level and suppresses the common mode source noise peaks. To fully realize the potential noise reduction of spectrally balanced detection would require a single detector or hardware implementation to reduce the thermal and DAQ contribution by a factor of 2.

#### Acknowledgments

This research was supported in part by research grants from the National Institutes of Health (R01-RR019768 R01-EY014975) and the Department of Defense (F4 9620-01-1-0014).